Growth mechanism of subsurface hydrogen cavities in tungsten exposed to low-energy high-flux hydrogen plasma

Chen, Wanqi; Wang, X. Y. ; Chiu, Yu-Lung; Morgan, T.W.; Guo, W.G. ; Li, K.L.; Yuan, Y. ; Xu, B.; Liu, W.

DOI:
10.1016/j.actamat.2020.04.012

Document Version
Peer reviewed version

Citation for published version (Harvard):
Chen, W, Wang, XY, Chiu, Y-L, Morgan, TW, Guo, WG, Li, KL, Yuan, Y, Xu, B & Liu, W 2020, 'Growth mechanism of subsurface hydrogen cavities in tungsten exposed to low-energy high-flux hydrogen plasma', *Acta Materialia*, vol. 193, pp. 19-27. https://doi.org/10.1016/j.actamat.2020.04.012

Growth mechanism of subsurface hydrogen cavities in tungsten exposed to low-energy high-flux hydrogen plasma

W. Q. Chen[a,b], X. Y. Wang [a], Y. L. Chiu[b,*], T.W. Morgan[c], W. G. Guo[d], K. L. Li[a], Y. Yuan[d], B. Xu[a], W. Liu[a,**]

[a] School of Materials Science and Engineering, Tsinghua University, Beijing, 100084, PR China

[b] School of Metallurgy and Materials, University of Birmingham, Edgbaston, Birmingham B15 2TT, UK

[c] DIFFER-Dutch Institute for Fundamental Energy Research, De Zaale 20, 5612 AJ Eindhoven, Netherlands

[d] School of Physics, Beihang University, Beijing, 100191, PR China

*Corresponding Author: Tel: 86-010-62772852, Email: liuw@mail.tsinghua.edu.cn (W. Liu); Tel: 00-44-7954222327 Email: Y.Chiu@bham.ac.uk (Y. L. Chiu).

W. Q. Chen and X. Y. Wang contributes equally to this work. They are listed as co-first authors.

Abstract

Due to a lack of direct experimental results, the detailed mechanisms that govern the blistering behavior of tungsten (W) exposed to ITER-relevant condition in nuclear fusion remain unclear. The growth mechanism of hydrogen (H) blisters is one example. In this work, recrystallized W was exposed to H plasma at 50 eV, 1.5×10^{26} m^{-2}, and 573 K. Transmission electron microscopy (TEM) samples were prepared using plasma-focused ion beam (FIB) followed by flash-polishing to effectively remove surface damages induced by FIB. The TEM images revealed that the general blisters observed on the exposed surface are associated with underlying cavities. A considerable amount of dislocations were found in the vicinity of the cavities. Prismatic dislocation loop arrays were observed**,** including small size 'coffee-bean' prismatic loops and large size prismatic loops. Near the tip of surfaces cavities, evidences for the emission of shear loops were also found. Based on the experimental findings, a multi-stage growth mechanism of H cavities was proposed. The loop-punching mechanism is operative for both very small cavities and cavities with sizes larger than several hundreds of nanometers. Whereas at intermediate sizes, cavities grow by emitting shear loops from the cavity tip.

Keywords: tungsten, H plasma, blistering behavior, loop punching, shear loop emission

1. Introduction

Harsh service environment imposes great challenges for plasma facing materials (PFMs) in the divertor of fusion devices. With its favorable properties such as high

thermal conductivity, high melting temperature, and low sputtering yield, tungsten (W) has become a promising candidate for PFMs in the divertor of the International Thermonuclear Experimental Reactor (ITER) [1]. During ITER operations, W is exposed to a plasma of hydrogen (H) and its isotopes (deuterium and tritium) at low energy (from tens to hundreds of eV) and high fluxes (10^{22}–10^{24} ions/m^2·s), which poses many challenges for the PFMs. One issue for W is the retention of H isotopes. The resultant supersaturated H isotopes within W may cause severe blistering and surface modification even when the incident energy is below the threshold for displacement damage [2, 3]. Such blistering causes dramatic degradation in the mechanical properties (e.g. H-induced hardening and embrittlement [4, 5]) and thermal properties (e.g. decreased thermal conductivity). Moreover, the bursting of the H blisters triggers the formation of W flakes which may contaminate the core plasma and disturb the steady discharges. Therefore, understanding the blistering behavior in W is a key to the development of PFMs that can withstand the harsh environment inside the fusion reactor.

A cavity generally refers to either a void or a gas bubble beneath the surface. A void is an empty cavity that grows and shrinks by the absorption of vacancies. On the other hand, if the addition of gas causes the cavity to become spherical, the cavity could be considered a bubble. A blister refers to a void or gas bubble close to the sample surface, which can be observed by scanning electron microscopy (SEM) or optical microscopy [6, 7]. For H plasma exposure, blister means the dome-shape structure observable on the surface, usually associated with an underlying subsurface cavity

that could be confirmed by SEM views of the cross section prepared by focused ion beam (FIB) [2, 8, 9].

The surface blistering of W is generally linked to the cavity formation as a result of plastic deformation [3, 6, 10], dislocation loop punching [6, 11], agglomeration of H-vacancy complexes [12], and solute H isotope distribution [13]. Among them, plastic deformation and dislocation loop punching are widely regarded as the most common and trustworthy growth mechanisms of the sub-surface cavities (i.e. H-bubbles). The plastic deformation mechanism, which relates to the plastic deformation near the metal surface when small bubbles grow, has been reported as responsible for both inter- and intra-granular blisters [3, 14]. For inter-granular blisters, large cavities mainly arise at grain boundaries. The lateral elongation directions of high-dome blisters were found to coincide with <111> directions, which is attributed to the mechanical stress induced by H (or its isotopes) gas pressure in the cavity from the super-saturated bulk inventory [14]. Meanwhile, the intra-granular blisters are associated with the cavities inside individual grains. Based on the plastic deformation mechanism of W, a pronounced dependence of the blistering behavior on the crystal orientation has been widely acknowledged and used to explain the step-like structures of blisters observed [3]. Moreover, a few nanometer-scale experiments also revealed the plastic deformation during the blister formation [15-17]. According to TEM observations of W samples polished from one side, Dubinko et al. [15, 16] suggested that plasma irradiation would strongly increase the dislocation density. They claimed that high-heat flux plasma causes a strong temperature gradient and

stress distribution across the surface, and that the severe plastic deformation leading to the dislocation microstructure is a co-product of thermal stress and intensive plasma particle uptake mainly at the beginning of the exposure. They also observed individual 'coffee-bean' dislocation loop, and attributed it to the loop punching mechanism operating while the bubbles and cavities grow during continuous plasma exposure [16]. Unfortunately, a direct link between the dislocation microstructure and the cavity structure is still missing due to the limitations of the TEM sample fabrication method used. Thus, the underlying mechanism of blistering behavior remains unclear. Recently, Guo et al. [17] prepared TEM specimens by twin-jet electro-polishing with the plasma-exposed side protected with paraffin. They observed dislocation tangles formed in W after H plasma exposure, accompanied by intra-granular blisters. It was suggested that the dislocations migrate and interact with each other to form tangles or <001> edge dislocation, and this could be the initial nucleation mechanism of blisters. Substantial dislocations are expected to form via severe plastic deformation of the blister cap. However, those authors thought that the loop punching mechanism is not applicable during the blistering process, because they observed neither nanometer-scale bubbles nor dislocation loop arrays, contradicting the work of Dubinko et al. [16]. Therefore, further efforts are needed to thoroughly understand the blistering behavior, especially to clarify the existence of the loop punching mechanism.

Loop punching is a form of plastic deformation [6]. It refers to the process of self-interstitial atoms being driven out from the metal/cavity interface to form a

prismatic dislocation loop punching out from the interface. The main driving force for the loop punching mechanism is the hydrostatic stress induced by internal gas. According to Condon et al. [6], loop punching is the main mechanism for H bubble growth in multiple metals and alloys including Al and Cu, and it is frequently observed in the growth of helium (He) bubbles in W [18-21]. In the microstructure, the loop punching mechanism is accompanied by chains of nanometer-sized loops aligned along their Burgers vectors [6]. This mechanism may also be identified by the morphology of the cavity and surface blister, when the surface terrace mimics the internal cavity [14]. With such observations, loop punching is believed to be one of the main mechanisms for H cavity growth in W after an H_2 gas bubble nucleates at a vacancy cluster [22]. While the loop punching mechanism is a key assumption used in modeling work [23-25], its direct evidence such as the described dislocation loop arrays has not been reported.

Note that the lack of the experimental observations of micro- and nanometer-size blistering behavior makes it difficult to understand the growth mechanism of cavities. In this study, we utilized TEM techniques to characterize the damage microstructure in W induced by H plasma exposure. The flash polishing technique could effectively remove FIB-induced surface damage to enable detailed study of the dislocation microstructures of the samples. These microstructural features are necessary to elucidate the operative cavity growth mechanisms. In conjunction with the analysis using a continuum model, a multi-stage growth mechanism of the H cavity in W after H-plasma exposure is proposed.

2. Experimental

Polycrystalline W (99.99 wt% purity) was supplied by Plansee Gruppe, Austria and heat-treated under vacuum at 1873 K for 2 h after electro-polishing. The samples were exposed to a high-flux H plasma beam in the Magnum-PSI linear plasma device (DIFFER, Eindhoven, the Netherlands) for steady-state exposure in ITER-relevant conditions [26-28]. The electron temperature and density were measured by Thomson scattering. The H plasma flux was determined by the temperature of the plasma beam and controlled at about $2\text{–}3 \times 10^{23}\ \mathrm{m^{-2} \cdot s^{-1}}$. The total fluence was about $1.5 \times 10^{26}\ \mathrm{m^{-2}}$, and the ion energy was fixed at ~50 eV by negatively biasing the sample. A water cooling system was applied to the back side of the samples to control the surface temperature. In this work, the surface temperature was set at ~573 K.

A xenon plasma-FIB system (FEI Helios G4 CXe) was utilized to extract TEM lamellae from the irradiated W sample, in order to observe the cross-sectional foils parallel to the plasma exposure direction. Xe^+ plasma FIB has the advantage of inducing typically 20–40% less damage than Ga^+ FIB during the fabrication process [29, 30]. In order to remove the damaged layer on both sides of the lamellae caused by plasma FIB, a final flash polishing procedure was carried out at 14 V in and solution containing 0.5 wt% NaOH aqueous at 273 K for 10 ms. TEM microstructural observation was performed on an FEI Talos F200 microscope operated at 200 kV. The morphology of irradiated damage defects was detected under two-beam condition in the scanning transmission electron microscopy (STEM) mode.

3. Results

Fig. 1 provides the cross-sectional overview of a W sample after exposed to H plasma. The blisters observed on the exposed surface were directly linked with cavities beneath the surface, which were within 4 μm from the surface and typically of micro-cavity shapes with a length of 1 μm or less. Noticeable dislocations can be observed in the vicinity of the cavities, and the dislocation density rapidly decreases away from the cavities. Most dislocations located away from the cavities are aligned in arrays (or strings) that can be linearly linked to the cavities, suggesting that these dislocation loop arrays/strings may have originated from these cavities. There are two distinctive $\langle 111 \rangle$ directions ($[\bar{1}\bar{1}1]$ and $[\bar{1}11]$ as shown by the white arrows in Fig. 1) along which most of the dislocation loop arrays are aligned. Dislocations as far as 11 μm away from the exposed surface can be observed.

Fig. 2 are the enlarged images of the left side in Fig. 1, with the typical morphology of large-scale dislocation loops distributed around the cavities. Fig. 2 (a) shows the length of cavities is larger than 500 nm, with the nearby dislocation loops presumably emitted from the cavities. The enlarged views of areas 1–4 in Fig. 2 are depicted in Figs. 2 (b)–(e), respectively. In order to conduct Burgers vector analysis of these dislocation loops, the $\boldsymbol{g}\cdot\boldsymbol{b}$ = 0 invisibility criterion was applied. The adopted diffraction vectors are $\boldsymbol{g}_1 = 020$, $\boldsymbol{g}_2 = 10\bar{1}$, $\boldsymbol{g}_3 = 01\bar{1}$, and $\boldsymbol{g}_4 = 1\bar{1}0$. When the dislocations of interest are out of contrast, the diffraction vector $\boldsymbol{g}$ is marked in yellow color. The dislocation loops in areas 1 and 3 are invisible with $\boldsymbol{g}_4 = 1\bar{1}0$, indicating that their Burgers vectors are $\boldsymbol{b}_1 = \boldsymbol{b}_3 = \pm\frac{1}{2}[11\bar{1}]$. Coincidentally, the invisible

conditions of the dislocation loops in areas 2 and 4 are also the same, which means that their Burgers vectors are $\boldsymbol{b}_2 = \boldsymbol{b}_4 = \pm\frac{1}{2}[\bar{1}11]$. According to Fig. 2, these dislocation loops are edge dislocation loops (ie. prismatic loops). The string of arrayed dislocation loops in W under H plasma exposure was experimentally observed here for the first time.

Small size dislocation loops with a typical 'coffee-bean' shape were also observed after the plasma exposure. Fig. 3 shows a chain of 'coffee-bean' dislocation loops near the large-scale dislocation loops in area 1 (depicted in Fig. 2 (b)). Both types of dislocation loops have the same Burgers vector $\boldsymbol{b_5} = \boldsymbol{b}_1 = \pm\frac{1}{2}[11\bar{1}]$. These prismatic loops are also arranged along the $[\bar{1}\bar{1}1]$ direction, which is the same as the loops distributed in area 1 in Figs. 1&2.

Besides, individual 'coffee-bean' loops were observed near the cavity beneath the surface, as shown in Fig. 4. According to the $\boldsymbol{g} \cdot \boldsymbol{b} = 0$ criterion, the Burgers vector is $\boldsymbol{b_6} = \pm\frac{1}{2}[1\bar{1}1]$. Other studies also reported the existence of the individual 'coffee-bean' loop [16]. We tend to believe the individual 'coffee-bean' loop originates from the interactions between dislocations because of its separate occurrence.

Fig.5 shows an array of dislocation observed in another grain exhibited different features from the prismatic loops mentioned above. The length of cavities in this grain is found to be about 200-500 nm, which is apparently smaller than the cavities observed in Figs.2-4. According to $\boldsymbol{g} \cdot \boldsymbol{b} = 0$ invisibility criterion, their Burgers vector is $\boldsymbol{b_7} = \pm\frac{1}{2}[1\bar{1}1]$. As shown in Figs. 5(a) and (b), the arrayed dislocation loops exhibit typical features as dots or short strings aligned along $[1\bar{1}1]$ direction, indicating that the dislocation loops are along the slip plane which is parallel to the beam direction z=[011]. Thus, the dislocation loop plane can be confirmed to be

$(21\bar{1})$. In other words, these dislocation loops are shear loops on $(21\bar{1})$ plane with Burgers vector $= \pm\frac{1}{2}[1\bar{1}1]$.

Therefore the current TEM observations confirm the existence of both prismatic dislocation loops and shear dislocation loops, consistence with the loop punch mechanism and the shear loop emission mechanism. These two mechanisms will be discussed in the following section, in relation to the cavity growth.

4. Discussion

In order to figure out the growth mechanism of the in-grain H cavity in W, one usually needs to examine the morphology of the cavity [31] and dislocations nearby. According to Kolasinki et al. [25], the shape of the cavity can be determined by the growth mechanism. In the present study, the observed dislocations in the flash-polished sample may also shed light on the different growth mechanisms of cavities. Most of the dislocations observed under TEM are correlated with (or in the vicinity of) the cavity. However, the cavities are not the only source of dislocations in W. A high-heat flux plasma will also cause a strong thermal gradient via fast heating of the surface, which consequently leads to inhomogeneous stress with the highest gradient at the top surface. It is conceivable that, prior to the appearance of H cavities, numerous dislocations have occurred under the plastic deformation induced by the high stress gradient [16]. However, the main concern in this study is the growth mechanism of the cavities, not the initial dislocation sources. The perspective of growth mechanism is based on TEM observations that the dislocations are distributed around the cavities in the near-surface. Thus, here the “growth mechanism” refers to

mechanical deformation of the metal during the growth of the cavities irrespective of the initial nucleation process. Besides, it is pertinent to point out that the dislocations are distributed both near and away from the cavities. The maximum depth of dislocations is three times more than the location depth of cavities. The salient feature is ascribed to the movement and propagation of dislocations during the growth of cavities.

Based on the experimental results, it could be inferred that both the loop punching and shear loop emission from the cavity tip exist during the growth process of cavities. These two mechanisms are expected to produce dislocations with different distribution patterns: the loop punching mechanism only produces chains of prismatic loops with the same Burgers vector, while the shear loops emitted from the cavity tip are usually located near the cavity. It is important to explore the factors determining which mechanism is activated and/or dominant. In order to explain the salient feature of cavities and dislocations observed by TEM, below we will apply a continuum scale model to analyze the growth mechanism of cavities with varying morphologies at different stages.

4.1 Loop punching mechanism

The observation of chains of prismatic dislocation loops in Fig. 2–4 indicates that the dislocation loop punching mechanism is a major one during the growth of H cavities.

Consider a small flat elliptical cavity with axis lengths of a, b, and c (Fig. 6 (a)) that grows by loop punching. For the flat ellipse, $a = b > c$, and the axis ratio $k = a/c$ is the

major variable determining the shape of the ellipse.

For the elliptical cavity, the energy to form a dislocation loop is given by [31]:

$$E = L\left(\frac{\mu|\overrightarrow{b}|^2}{4\pi}\right)\ln\left(\frac{r_0}{r_p}\right) \quad (1)$$

In equation (1), L is the circuit length of the punched-out loop, $|\vec{b}|$ is the length of Burgers vector, r_0 is the length of the dislocation source, while r_p is the distance at which the dislocation loop can be punched out. According to the theoretical study by Greenwood et al. [31], $r_0 \approx a$ and $r_p \approx |\vec{b}|$. L equals to the perimeter of the cross section of the elliptical bubble in the dislocation loop direction, and it can be evaluated by type II elliptical integration:

$$L = \int_0^1 4a\sqrt{\frac{1-e^2t^2}{1-t^2}}\,dt \quad (2)$$

$$e = \sqrt{1-\frac{b^2}{a^2\sin^2\theta+b^2\cos^2\theta}} = \sqrt{1-\frac{1}{k^2\sin^2\theta+cos^2\theta}} \quad (3)$$

θ is the angle between the loop Burgers vector and the long axis of the elliptical bubble.

The free energy change to produce the dislocation loop can be expressed as:

$$\mathrm{d}F = -(p-p_e)\mathrm{d}V = -(p-p_e)S(\theta)\,\overrightarrow{|b|} \quad (4)$$

$S(\theta)$ is the cross-sectional area of the elliptical bubble, and p_e is the pressure difference between the inside and outside.

According to Young-Laplace theorem [32],

$$\gamma\mathrm{d}A = p\mathrm{d}V \quad (5)$$

and when using the following approximations for the surface area and volume of an ellipsoid:

$$A = 4/3\pi(ab+bc+ac) \quad (6)$$

$$V = 4/3\pi(abc) \tag{7}$$

We can obtain

$$p_e = \frac{2}{3}\gamma\left(\frac{2}{a}+\frac{1}{c}\right) \tag{8}$$

For the spontaneous punching-out of a dislocation loop, the system energy should satisfy $dF + E < 0$, then p satisfies:

$$p > \frac{1}{a}\left[\frac{\mu|\vec{b}|L(a,\theta)}{4\pi a} ln\left(\frac{a}{|\vec{b}|}\right)\frac{1}{\sqrt{\cos^2\theta+\frac{1}{k^2}\sin^2\theta}} + \frac{2}{3}\gamma(2+k)\right] \tag{9}$$

the loop can be spontaneously punched out.

As a special case of the elliptical cavity, when k=1, which represents a spherical bubble, the equation can be roughly evaluated by the well-known form of loop punching pressure [31],

$$p > (2\gamma + \mu|\vec{b}|)/a \tag{10}$$

In bcc W, only loops with the Burgers vector $\vec{b} = \frac{1}{2}\langle 111\rangle$ can be punched out. Assuming the long and short axis directions of the elliptical bubble are aligned along $\langle 100\rangle$ and $\langle 001\rangle$, respectively, then $\theta = \tan^{-1}\left(\frac{1}{\sqrt{2}}\right) = 35.26°$, and the pressure required for loop punching with different cavity sizes and axis ratios is shown in Fig. 7.

It is clearly shown in Fig.7 that the loop punching threshold pressure decreases for larger cavities [31, 33]. However, the non-monotonic behavior of the threshold pressure with the change of axis ratio k is due to the competition between the decreasing loop size and the increasing specific surface area. With increasing axis ratio, the pressure first decreases as a result of reduced loop perimeter (the integral $L(a,\theta)$in Eq. 2). Then, with higher k values the pressure increases almost linearly

with *k*, which is attributed to the increased specific surface area of the bubble. With a greater *k*, the bubble needs to overcome a higher surface energy for each unit volume it gains. Thus, it can be inferred that for flat cavities with large *k* values or crack-like bubbles with sharp tips, the great required loop punching pressure makes this mechanism unfavorable.

A similar situation has been reported by molecular dynamics simulations for the growth of He bubbles in W. The He bubbles were found to grow by pushing out W self-interstitial atoms and rearranging into a prismatic dislocation loop with a Burgers vector of $\boldsymbol{b} = \pm\frac{1}{2}\langle 111\rangle$, and the loop moves away from the bubble along the $\langle 111\rangle$ direction once the number of self-interstitial atoms exceeds the threshold [19, 34, 35]. While that worked well for the case of nanometer-scale He bubbles, the situation is dramatically different for H cavities observed in our study, mainly in the shape of the subsurface cavity. Unlike the spherical He bubbles, the H cavities have a crack-like structure with a wide size range in their nearby loops (as shown in Fig. 2). Therefore, the mechanism responsible for the growth of H cavities in this study should be more complicated than the general loop punching mechanism suggested for He bubbles. Notably, another growth mechanism of the H cavity here is the emission of shear loops from the cavity tip.

4.2 Shear loop emission from the cavity tip

Fig. 5 shows a typical case of cavity growth by the emission of shear dislocation loops, below is the analysis of this mechanism.

For shear loop emission from the edge of an elliptical cavity, the cavity can also be

assumed as a round-tip elliptical crack that is expanding with internal load. According to Huang et al. [36], the force needed to emit a dislocation near a rounded-tip cavity is:

$$|\vec{b}|\tau_{\rho\theta} = |\vec{b}|K_{\mathrm{I}}(8\pi r)^{-\frac{1}{2}}\sin\left(\frac{\theta}{2}\right)(1+\cos\theta+\frac{\rho}{r}) \tag{11}$$

K_{I} refers to the generalized mode I cavity stress intensity factor, assuming that the blunt cavity is replaced by a sharp cavity at the curvature center [37]. The schematic is shown in Fig. 6. The combination of (θ, r) denotes the position in a radial coordinate system, and ρ is the curvature radius of the rounded cavity tip.

Note that the exact geometry of the cavity-tip region on the atomic scale is hard to determine, even though the overall cavity shape is considered flat elliptical. Moreover, the TEM results shed no light on the structure at the cavity tip. Thus, when considering shear loop emission from the cavity tip, ρ is assumed to be an independent variable not affected by the overall shape of the cavity.

Meanwhile, for a sharp elliptical cavity, the stress intensity factor K_{I} is given by [38]:

$$K_{\mathrm{I}} = 2p\sqrt{a/\pi} \tag{12}$$

This assumption was also used in the finite element analysis by Li et al. [39].

The main resistance against the emission of shear loop is the image force and the ledge force:

$$f_{\mathrm{image}} = -\frac{\mu|\vec{b}|^2}{4\pi(1-\nu)r} \tag{13}$$

$$f_{\mathrm{ledge}} = -\frac{2}{\pi}\frac{\gamma\eta|\vec{b}|sin\beta}{\eta^2+r^2} \tag{14}$$

$$\eta = \frac{1}{2}e^{\frac{3}{2}}\mathrm{r} \tag{15}$$

Both forces are resistance for shear loop emission. r refers to the distance between of the emitted shear dislocation loop and the cavity tip. There is a threshold value ξ_0 (when $r > \xi_0$, the shear loop can be emitted) that is material dependent.

In real situations, according to Zhu et al. [40] a dislocation is usually emitted from the cavity tip or nearby source in the form of gradually expanding shear dislocation loop (instead of a prismatic loop). Only when the dislocation loop expands to a certain extent can it be emitted from the cavity-tip successfully. The activation of the shear loop emission requires the loop size to be large enough, so that the segments within can overcome the image force. According to Rice et al. [41], the radius of active loop in W is around $\xi_0 = 50|\vec{b}|$. Thus, we use the approximation $\xi_0 = 50|\vec{b}|$ in Eq. 13.

When the emit force is greater than the resistance for the dislocation, the stress satisfies:

$$\tau_{r\theta} = 2p\sqrt{a/\pi}(8\pi(\xi_0 + r_d))^{-\frac{1}{2}} \sin\left(\frac{\theta}{2}\right)(1 + \cos\theta + \frac{\rho}{(r_d+\xi_0)}) > \frac{\mu b^2}{4\pi(1-\nu)\xi_0} + \frac{2}{\pi}\frac{\gamma\eta sin\beta}{\eta^2+{\xi_0}^2} \quad (16)$$

In which:

$$r_d \approx \rho \quad (17)$$

$\tau_{r\theta}$ can then be simplified as:

$$\tau_{r\theta} = \frac{p}{\sqrt{2}\,\pi}\sqrt{\frac{\xi+\rho}{a}} \sin\left(\frac{\theta}{2}\right)(1 + \cos\theta + \frac{\rho}{(\rho+\xi_0)}) > \frac{\mu b}{4\pi(1-\nu)\xi_0} + \frac{2}{\pi}\frac{\gamma\eta sin\beta}{\eta^2+{\xi_0}^2} \quad (18)$$

And the corresponding p is

$$p > \frac{\sqrt{\frac{\xi_0+\rho}{a}}}{\sin\left(\frac{\theta}{2}\right)(1+\cos\theta+\frac{\rho}{\xi_0+\rho})}\left(\frac{\sqrt{2}\mu b}{4(1-\nu)\xi_0} + \frac{2\sqrt{2}\gamma\eta sin\beta}{\eta^2+{\xi_0}^2}\right) \quad (19)$$

In this model, the required stress for dislocation loop punching in the H cavity in Fig. 4(a) (the size of the cavity is around 1 μm, and the axis ratio is around 25) is ~150 MPa, while the corresponding threshold pressure is ~330 MPa. Apparently, with

this length scale and cavity morphology, the loop punching mechanism is favored. Moreover, the shape of the surface cavity resembles that governed by loop punching mechanism according to Ref. [25]

We depict the pressure required for shear loop emission from the tip of the cavity in W in Fig. 7. The figure also compares the pressures for loop punching and shear loop emission.

4.3 Competition between the two mechanisms

Fig. 8 shows the required internal gas pressure for both the loop punching and the shear loop emission mechanisms for cavities with sizes over 50 nm. For smaller cavities, the pressure required for the shear loop emission is relatively lower, and therefore this mechanism will be the first to activate. As the cavity grows, the pressure required for both mechanisms will decrease, but the decrease rate is higher for the loop punching mechanism. For an elliptical cavity with k = 100, the loop punching mechanism is activated when the cavity size is beyond a critical length of 100–150 nm, depending on the curvature radius at the cavity tip. Increasing k value will increase the critical length: for k = 500 the critical length is around 250–400 nm.

Note that the above model is valid only when the dislocation source could produce a sufficiently large shear loop to activate the emission process. Therefore, when the size of cavity is smaller than the activated loop radius ($50|\vec{b}|\approx$13 nm), the above-mentioned shear loop emission model does not apply. In general, when the size of cavity is smaller than the radius of the activated loop, the ξ_0 value must be comparable to the cavity size. Here, we simply assume ξ_0 to be small compared to

the bubble size a, as shown in Fig. 5(c).

$$\xi_0 = r'a \tag{20}$$

and $r' < 1$.

The required gas pressure for shear loop emission from small cavities is depicted in Fig. 8. It is obvious that very small cavities are dominated by the loop punching mechanism. With growth of the cavity, the shear loop emission mechanism becomes more favored when the cavity size exceeds ~10 nm.

Based on the theoretical analysis results, we found that the loop punching mechanism is favored over the shear loop emission mechanism in two types of cavities: very small ones (<13 nm) that cannot produce a large enough activated shear loop, and large ones exceeding the critical cavity size. Meanwhile, shear loop emission is favored in the medium sized cavities. This finding may also explain the simultaneous existence of large arrayed prismatic loops and arrayed small 'coffee-bean' loops in Fig. 3, while the loops with intermediate sizes are missing.

In the experimental observation, the shear loop mechanism is characterized by the chain of prismatic loops with similar sizes to the cavity. These loops have very high diffusivities and may move far away from the cavity under thermal activation. Dislocation emitted from the crack tip, however, cannot diffuse without external load or excess gas pressure. The emit force on a shear loop decreases with increasing $\sqrt{r}$ (neglecting the $\frac{\rho}{r^{\frac{3}{2}}}$ term in eq. (11)). Considering the constant friction force, the emitted shear loop may not get far away. A complex dislocation network may form as a result of the emission of shear loops with different Burgers vectors and the

interaction between them [33]. Dislocation reaction within the networks may leave behind separate 'coffee-bean' dislocation loops, which are also observed in the experiment. Thus, we suggest that the experimentally observed dislocation configurations in the microstructure is probably due to a multi-stage growth process of H cavity: (1) When the sizes of the cavities are very small, they grow mainly by loop punching mechanism. Since the punched-out loop may not exceed the size of the cavity, this mechanism leaves behind arrayed 'coffee-bean' loops. (2) At intermediate sizes, the cavities grow mainly by the shear loop emission mechanism, which resembles the development of plastic crack. At this stage, dislocations are primarily series of gradually expanding shear loops, which may easily get entangled near the cavity. (3) At large sizes, the cavities grow by loop punching mechanism again. The punching-out loops can be observed as large-size arrayed prismatic loops.

Conclusions

In this study, explicit cross-sectional view of the blistering morphology in W after exposure to low-energy high-flux H plasma was achieved by dedicated TEM sample fabrication. The cavities observed on the surface are associated with the cavities beneath the surface. A considerable amount of dislocations was distributed in the vicinity of the cavities. More specifically, small-scale 'coffee-bean' prismatic dislocation loop string, a few chains of large-scale prismatic dislocation loops, and shear loops were observed experimentally for the first time.

An integrated mechanism was put forward to explain the growth of the cavities,

based on cavity-tip induced shear loop emission and loop punching. With increasing cavity size, the growth process could be divided into three stages. Firstly, loop punching occurs for the nanometer-sized bubbles due to the ultra-high internal pressure, forming the small-scale 'coffee-bean' prismatic loop string. Secondly, the shear loop emission mechanism is taken as a result of increasing length of dislocation source and active shear loop size. This coincides with the appearance of shear loops arrayed at the tip of the cavity. Thirdly, further increase in the cavity size would again favor the loop punching mechanism, which is consistent with the observation of the large-scale arrayed prismatic loops. The H cavities, with their high axis ratio and low curvature radius at the tip (crack-like), favor the shear loop emission mechanism. On the contrary, H cavities with a low axis ratio and a high curvature radius (bubble-like) are more prone to have the loop punching mechanism.

This study utilized both experimental and theoretical methods to provide new insights into the underlying mechanism of blistering behavior. Furthermore, we obtained essential information about the methodologies in research of the microstructural evolution in PFMs, which is of vital importance for the development of nuclear fusion.

Acknowledgments

This work was supported by National Nature Science Foundation of China under Contract No. 51971115, and the Tsinghua Scholarship for Overseas Graduate Studies. This work has been carried out within the framework of the EURO fusion Consortium

and has received funding from the Euratom research and training programme 2014–2018 and 2019–2020 under grant agreement No 633053. The views and opinions expressed herein do not necessarily reflect those of the European Commission. DIFFER is a partner in the Trilateral Euregio Cluster (TEC). The technical supports from the Center for Electron Microscopy of the University of Birmingham, UK are acknowledged. W. Q. Chen is grateful for valuable supports on TEM and plasma-FIB techniques from Dr. Shanshan Si, Dr. Minshi Wang, and Dr. Xinyu Lu from the University of Birmingham. The help of Dr. Robin Schaeublin of ETHZ Switzerland on the flash-polishing work is gratefully acknowledged.

References

[1] T. Hirai, F. Escourbiac, S. Carpentier-Chouchana, A. Durocher, A. Fedosov, L. Ferrand, T. Jokinen, V. Komarov, M. Merola, R. Mitteau, R.A. Pitts, W. Shu, M. Sugihara, V. Barabash, V. Kuznetsov, B. Riccardi, S. Suzuki, ITER full tungsten divertor qualification program and progress, Phys. Scr. T159 (2014) 014006.

[2] Y.Z. Jia, G. De Temmerman, G.N. Luo, H.Y. Xu, C. Li, B.Q. Fu, W. Liu, Surface morphology and deuterium retention in tungsten exposed to high flux D plasma at high temperatures, J. Nucl. Mater. 457 (2015) 213-219.

[3] Y.Z. Jia, W. Liu, B. Xu, G.N. Luo, S.L. Qu, T.W. Morgan, G. De Temmerman, Mechanism for orientation dependence of blisters on W surface exposed to D plasma at low temperature, J. Nucl. Mater. 477 (2016) 165-171.

[4] W.Q. Chen, X.Z. Xiao, B. Pang, S.S. Si, Y.Z. Jia, B. Xu, T.W. Morgan, W. Liu, Y.L. Chiu, Irradiation hardening induced by blistering in tungsten due to low-energy high flux hydrogen plasma exposure, J. Nucl. Mater. 522 (2019) 11-18.

[5] M. Nagumo, Fundamentals of Hydrogen Embrittlement, Springer-Verlag Singapore Pte Ltd, Singapore, 2016.

[6] J.B. Condon, T. Schober, Hydrogen bubbles in metals, J. Nucl. Mater. 207 (1993) 1-24.

[7] G.S. Was, Fundamental of radiation materials science, Springer, New York, 2017.

[8] W.M. Shu, High-dome blisters formed by deuterium-induced local superplasticity, Appl. Phys. Lett. 92(21) (2008) 211904.

[9] M. Balden, S. Lindig, A. Manhard, J.-H. You, D2 gas-filled blisters on

deuterium-bombarded tungsten, J. Nucl. Mater. 414(1) (2011) 69-72.

[10] V.K. Alimov, J. Roth, M. Mayer, Depth distribution of deuterium in single- and polycrystalline tungsten up to depths of several micrometers, J. Nucl. Mater. 337(1-3) (2005) 619-623.

[11] W. Hu, F. Luo, Z. Shen, L. Guo, Z. Zheng, Y. Wen, Y. Ren, Hydrogen bubble formation and evolution in tungsten under different hydrogen irradiation conditions, Fusion Eng. Des. 90 (2015) 23-28.

[12] Y.-N. Liu, T. Ahlgren, L. Bukonte, K. Nordlund, X. Shu, Y. Yu, X.-C. Li, G.-H. Lu, Mechanism of vacancy formation induced by hydrogen in tungsten, AIP Adv. 3(12) (2013) 122111.

[13] L. Gao, A. Manhard, W. Jacob, U. von Toussaint, M. Balden, K. Schmid, High-flux hydrogen irradiation-induced cracking of tungsten reproduced by low-flux plasma exposure, Nucl. Fusion 59 (2019) 056023.

[14] S. Lindig, M. Balden, V. Kh Alimov, T. Yamanishi, W.M. Shu, J. Roth, Subsurface morphology changes due to deuterium bombardment of tungsten, Phys. Scr. T138 (2009) 014040.

[15] A.V. Dubinko, D.A. Terentyev, E.E. Zhurkin, Study of the Microstructure Induced by High-Flux Plasma via Transmission Electron Microscopy, J. Surf. Invest. X-ray Synchrotron Neutron Tech. 12(4) (2018) 792-796.

[16] A. Dubinko, D. Terentyev, A. Bakaeva, M. Hernandez-Mayoral, G. De Temmerman, L. Buzi, J.M. Noterdaeme, B. Unterberg, Sub-surface microstructure of single and polycrystalline tungsten after high flux plasma exposure studied by TEM, Appl. Surf. Sci. 393 (2017) 330-339.

[17] W. Guo, L. Ge, Y. Yuan, L. Cheng, S. Wang, X. Zhang, G.-H. Lu, (001) edge dislocation nucleation mechanism of surface blistering in tungsten exposed to deuterium plasma, Nucl. Fusion 59 (2019) 026005.

[18] L. Sandoval, D. Perez, B.P. Uberuaga, A.F. Voter, Competing Kinetics and He Bubble Morphology in W, Phys. Rev. Lett. 114(10) (2015) 105502

[19] H.X. Xie, N. Gao, K. Xu, G.H. Lu, T. Yu, F.X. Yin, A new loop-punching mechanism for helium bubble growth in tungsten, Acta Mater. 141 (2017) 10-17.

[20] X.C. Li, Y.N. Liu, Y. Yu, G.N. Luo, X.L. Shu, G.H. Lu, Helium defects interactions and mechanism of helium bubble growth in tungsten: A molecular dynamics simulation, J. Nucl. Mater. 451(1-3) (2014) 356-360.

[21] Y. Dai, G.R. Odette, T. Yamamoto, The Effects of Helium in Irradiated Structural Alloys, Elsevier Science Bv, Amsterdam, 2012.

[22] J. Hou, X.S. Kong, X. Wu, J. Song, C.S. Liu, Predictive model of hydrogen trapping and bubbling in nanovoids in bcc metals, Nat. Mater. 18 (2019) 833-839.

[23] R.D. Kolasinski, M. Shimada, Y. Oya, D.A. Buchenauer, T. Chikada, D.F. Cowgill, D.C. Donovan, R.W. Friddle, K. Michibayashi, M. Sato, A multi-technique analysis of deuterium trapping and near-surface precipitate growth in plasma-exposed tungsten, J. Appl. Phys. 118(7) (2015) 13.

[24] R.D. Kolasinski, D.F. Cowgill, D.C. Donovan, M. Shimada, W.R. Wampler, Mechanisms of gas precipitation in plasma-exposed tungsten, J. Nucl. Mater. 438 (2013) S1019-S1022.

[25] R.D. Kolasinski, D.F. Cowgill, R.A. Causey, A continuum-scale model of hydrogen precipitate growth in tungsten plasma-facing materials, J. Nucl. Mater. 415(1) (2011) S676-S679.

[26] A.S. Kukushkin, H.D. Pacher, A. Loarte, V. Komarov, V. Kotov, M. Merola, G.W. Pacher, D. Reiter, Analysis of performance of the optimized divertor in ITER, Nucl. Fusion 49(7) (2009) 075008.

[27] G.G. van Eden, M.L. Reinke, S. Brons, G. van der Bijl, B. Krijger, R. Lavrijsen, S.P. Huber, R. Perillo, M.C.M. van de Sanden, T.W. Morgan, Plasma radiation studies in Magnum-PSI using resistive bolometry, Nucl. Fusion 58(10) (2018) 106006.

[28] H.J.N. van Eck, G.R.A. Akkermans, S.A. van der Westen, D.U.B. Aussems, M. van Berkel, S. Brons, I.G.J. Classen, H.J. van der Meiden, T.W. Morgan, M.J. van de Pol, J. Scholten, J.W.M. Vernimmen, E.G.P. Vos, M.R. de Baar, High-fluence and high-flux performance characteristics of the superconducting Magnum-PSI linear plasma facility, Fusion Eng. Des. 142 (2019) 26-32.

[29] R.D. Kelley, K. Song, B. Van Leer, D. Wall, L. Kwakman, Xe+ FIB Milling and Measurement of Amorphous Silicon Damage, Microsc. microanal. 19(S2) (2013) 862-863.

[30] T.L. Burnett, R. Kelley, B. Winiarski, L. Contreras, M. Daly, A. Gholinia, M.G. Burke, P.J. Withers, Large volume serial section tomography by Xe Plasma FIB dual beam microscopy, Ultramicroscopy 161 (2016) 119-129.

[31] G.W. Greenwood, A.J.E. Foreman, D.E. Rimmer, The role of vacancies and dislocations in the nucleation and growth of gas bubbles in irradiated fissile material, J. Nucl. Mater. 1(4) (1959) 305-324.

[32] T. Young, III. An essay on the cohesion of fluids, 95 (1805) 65-87.

[33] H. Xie, G. Ning, X. Ke, G.H. Lu, Y. Tao, F. Yin, A new loop-punching mechanism for helium bubble growth in tungsten, 141 (2017) S1359645417307395.

[34] R. Kobayashi, T. Hattori, T. Tamura, S. Ogata, A molecular dynamics study on bubble growth in tungsten under helium irradiation, J. Nucl. Mater. 463 (2015) 1071-1074.

[35] J. Wang, L.-L. Niu, X. Shu, Y. Zhang, Energetics and kinetics unveiled on helium cluster growth in tungsten, Nucl. Fusion 55(9) (2015) 092003.

[36] M.X. Huang, Z.H. Li, Dislocation emission criterion from a blunt crack tip, J. Mech. Phys. Solids 52(9) (2004) 1991-2003.

[37] M. Creager, P.C. Paris, Elastic field equations for blunt cracks with reference to stress corrosion cracking, Int. J. Fract. Mech. 3 (1967) 247-252.

[38] P.C.I.H.P. H. Tada, G. R. Irwin, The Stress of Cracks Analysis Handbook, 3rd Ed, American Society of Mechanical Engineers Press, United States, 2000.

[39] M.Y. Li, J.H. You, Mechanics of tungsten blistering II: Analytical treatment and fracture mechanical assessment, J. Nucl. Mater. 465 (2015) 702-709.

[40] T. Zhu, J. Li, S. Yip, Atomistic configurations and energetics of crack extension in silicon, Phys. Rev. Lett. 93 (2004) 025503.

[41] S. Liang, Y.X. Zhu, M.S. Huang, Z.H. Li, Simulation on crack propagation vs. crack-tip dislocation emission by XFEM-based DDD scheme, Int. J. Plast. 114

(2019) 87-105.

Figure(s)

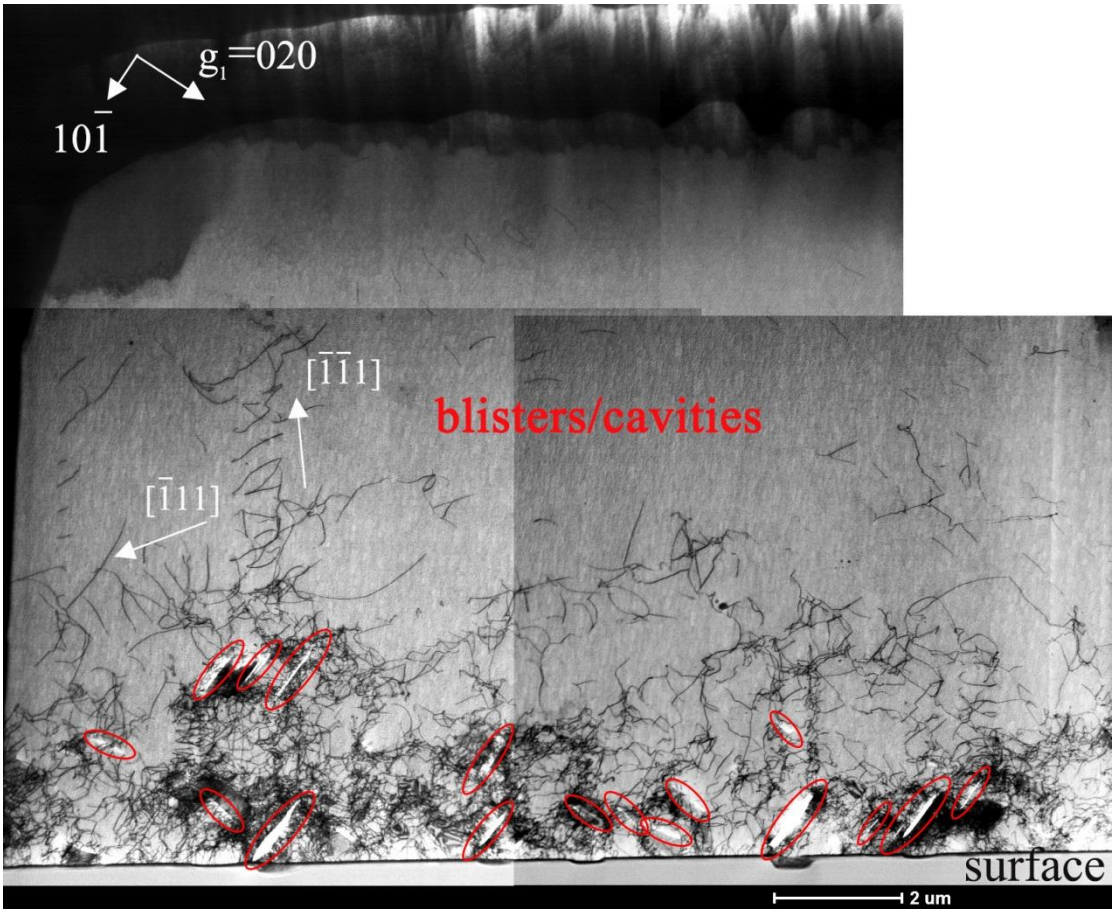

Fig. 1 An overview of the W microstructure after exposure to H plasma at 573 K. The bright field (BF)-STEM image was taken under the two-beam condition using the reflection g = 020. The cavities (marked by red circles) are located within 4 μm beneath the exposed surface, with visible dislocations around the cavities. Dislocations were observed as far as ~11 μm from the exposed surface. Most of the dislocation loop arrays are aligned along $[\bar{1}\bar{1}1]$ and $[\bar{1}11]$, which are labeled by white arrows.

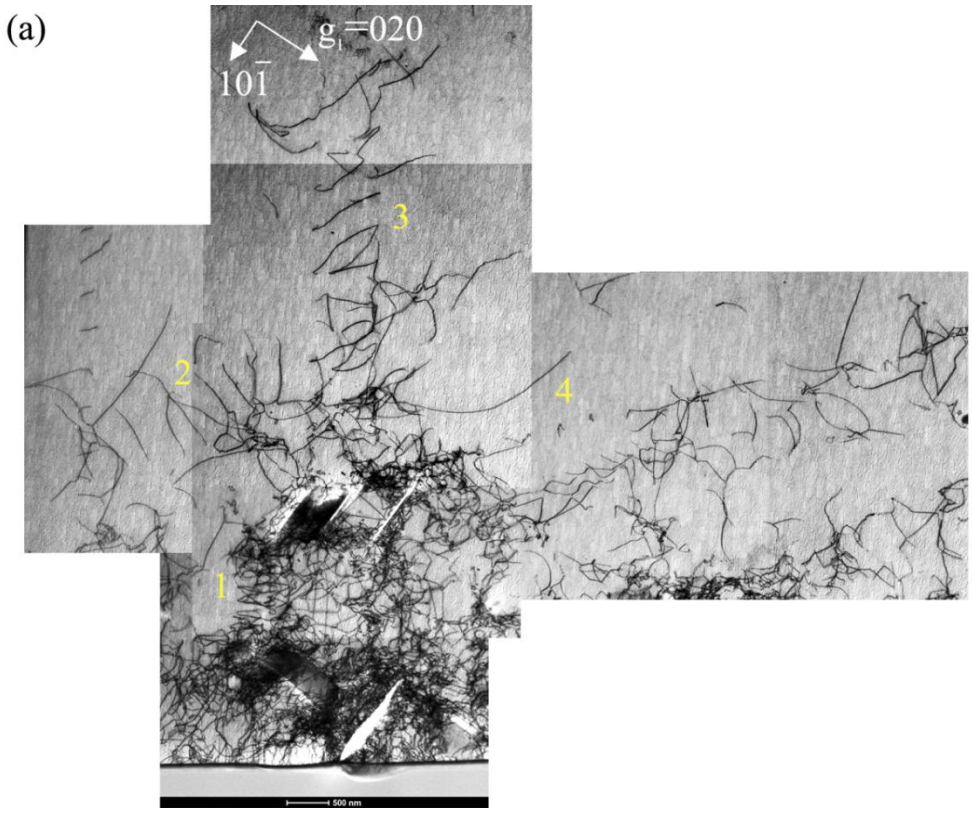
(a)
g_1=020
$10\bar{1}$
1
2
3
4
500 nm

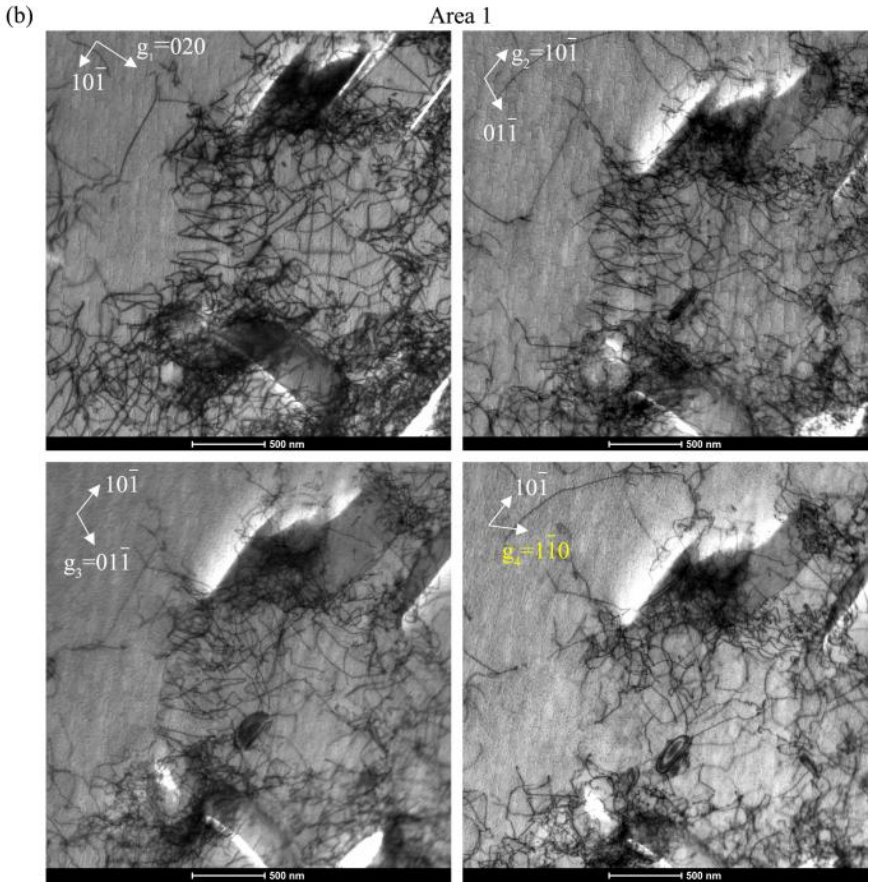
(b)
Area 1
g_1=020
$10\bar{1}$
g_2=$10\bar{1}$
$01\bar{1}$
$10\bar{1}$
g_3=$01\bar{1}$
$10\bar{1}$
g_4=$1\bar{1}0$
500 nm

(c) Area 2

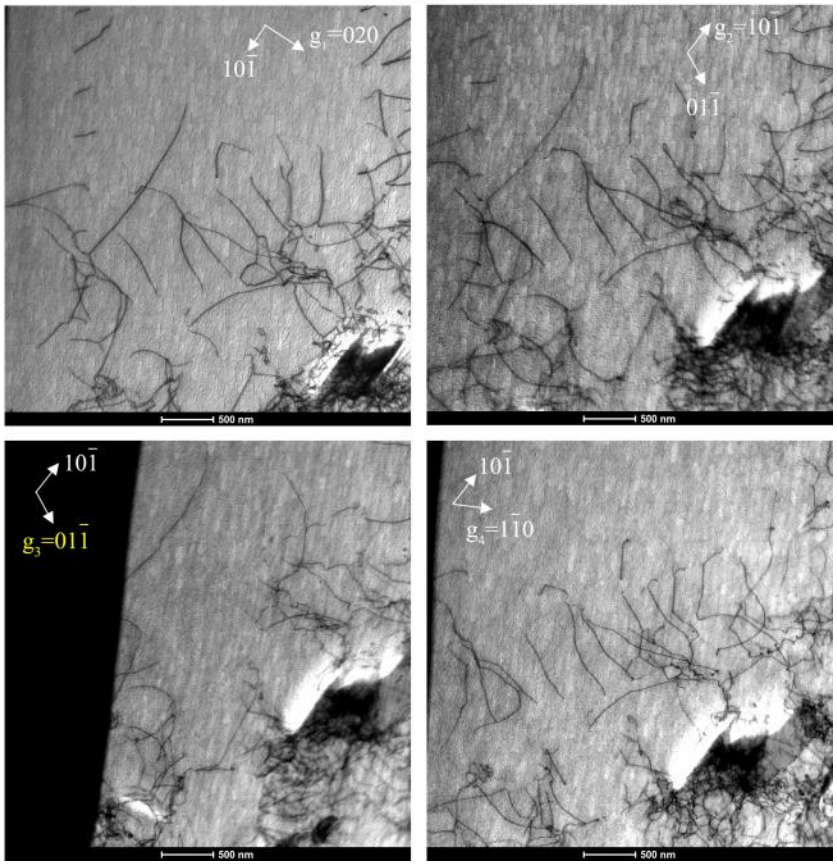

(d) Area 3

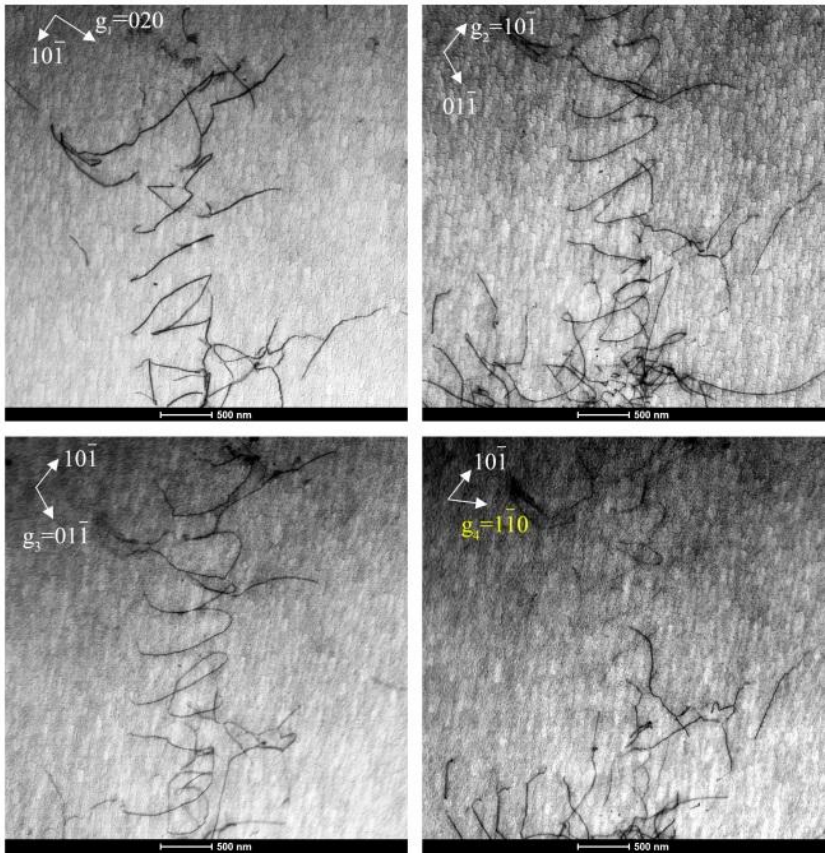

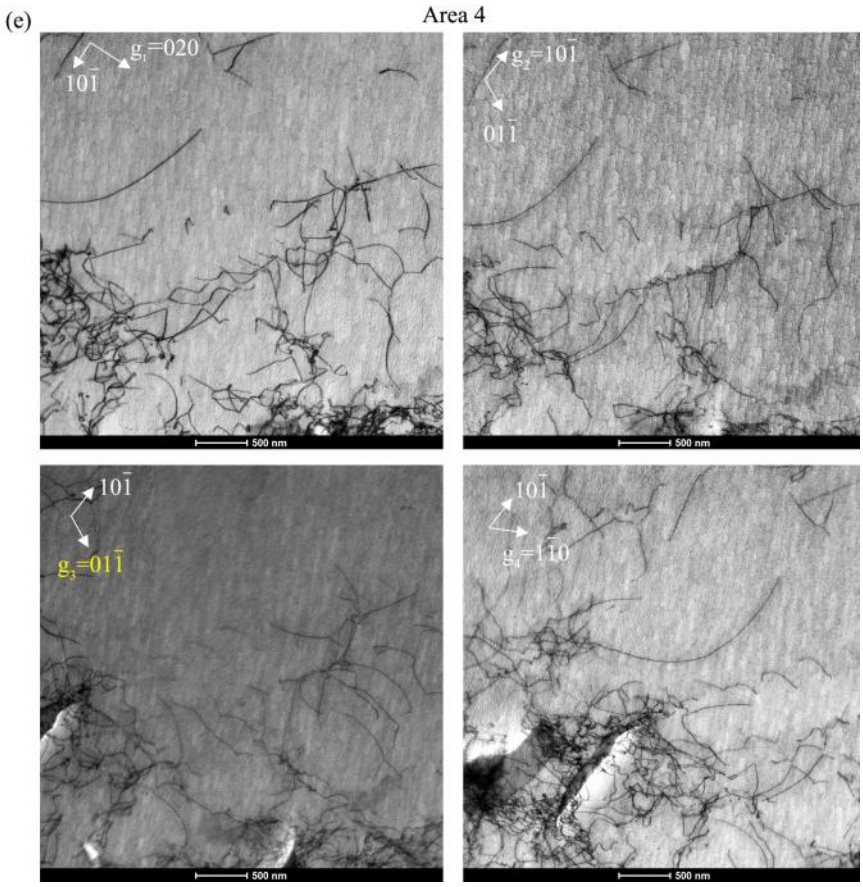

Fig. 2 (a) Typical morphology of dislocations (loops) distributed around the cavities. The length of the cavities is larger than 500 nm. (b)-(e) Enlarged images of areas 1–4 labelled in (a), respectively. The Burgers vector of the dislocation loops was identified by applying the $\boldsymbol{g} \cdot \boldsymbol{b} = 0$ criterion. The invisible condition was identified with the diffraction vector $\boldsymbol{g}$ highlighted in yellow color. The invisible diffraction conditions of areas 1 and 3 are the same, correspondingly, the Burgers vectors of the arrayed dislocation loops in areas 1 and 3 are both $\boldsymbol{b_1} = \boldsymbol{b_3} = \pm\frac{1}{2}[11\bar{1}]$. Meanwhile, the Burgers vectors of the dislocation loop arrays in areas 2 and 4 are the same as $\boldsymbol{b_2} = \boldsymbol{b_4} = \pm\frac{1}{2}[\bar{1}11]$.

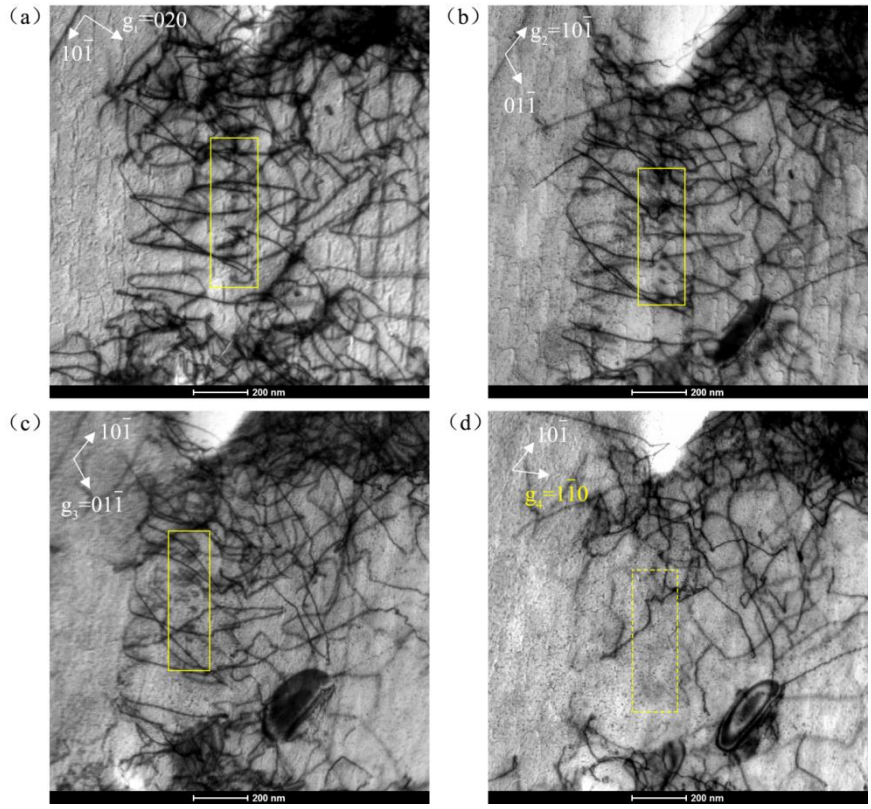

Fig. 3 A chain of 'coffee-bean' dislocation loops located in the vicinity of the large-scale arrayed dislocation loops (depicted in Fig. 2(b)). The Burgers vectors of these two types of prismatic loops features are both $\boldsymbol{b} = \pm\frac{1}{2}[11\bar{1}]$.

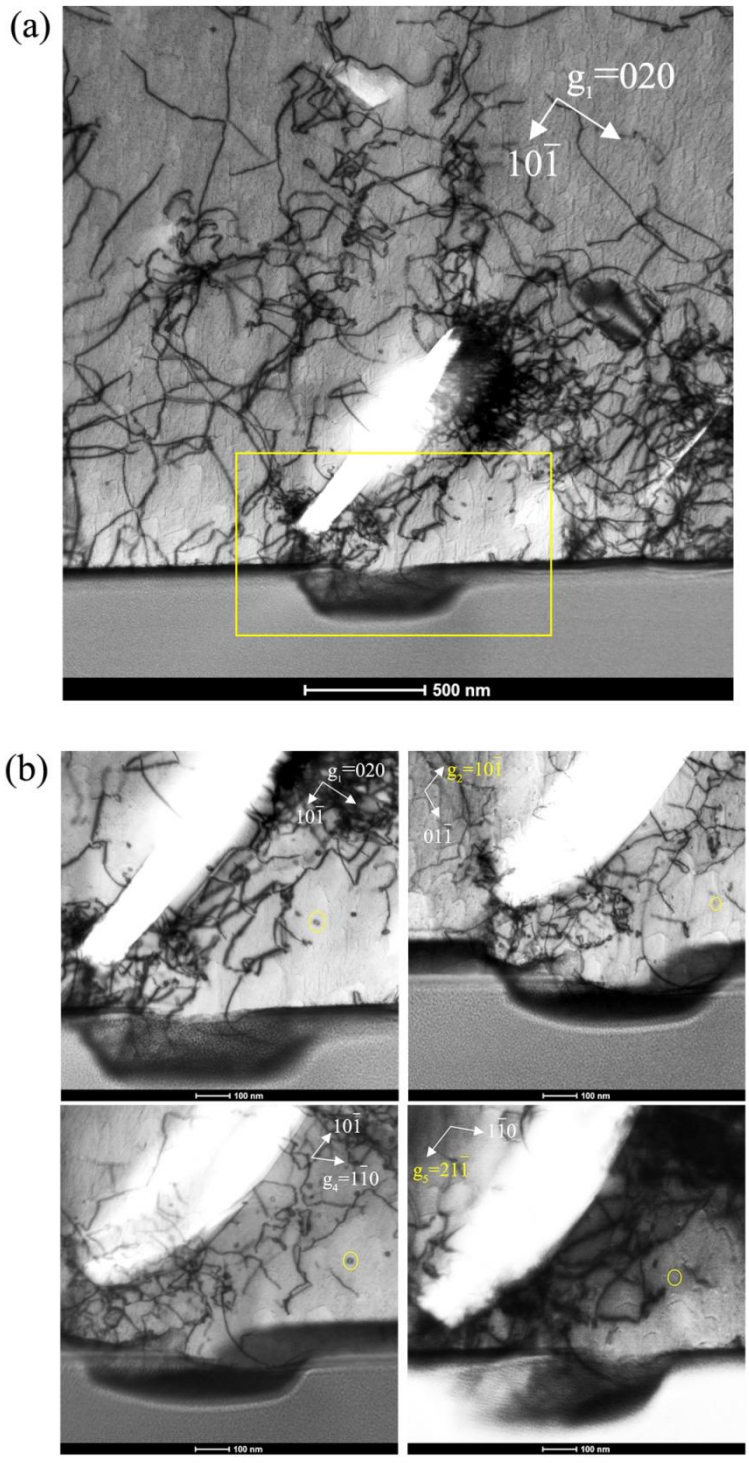

Fig. 4 (a) A distinct microstructure of the cavity located beneath the exposed surface. A considerable amount of dislocations was distributed in the vicinity of the cavity, with notable dense dislocation network at the tip of cavity. (b) Enlarged images illustrating the individual 'coffee-bean' dislocation loop located near the surface. According to the $\boldsymbol{g} \cdot \boldsymbol{b} = 0$ criterion, the Burgers vector is $\boldsymbol{b} = \pm\frac{1}{2}[1\bar{1}1]$.

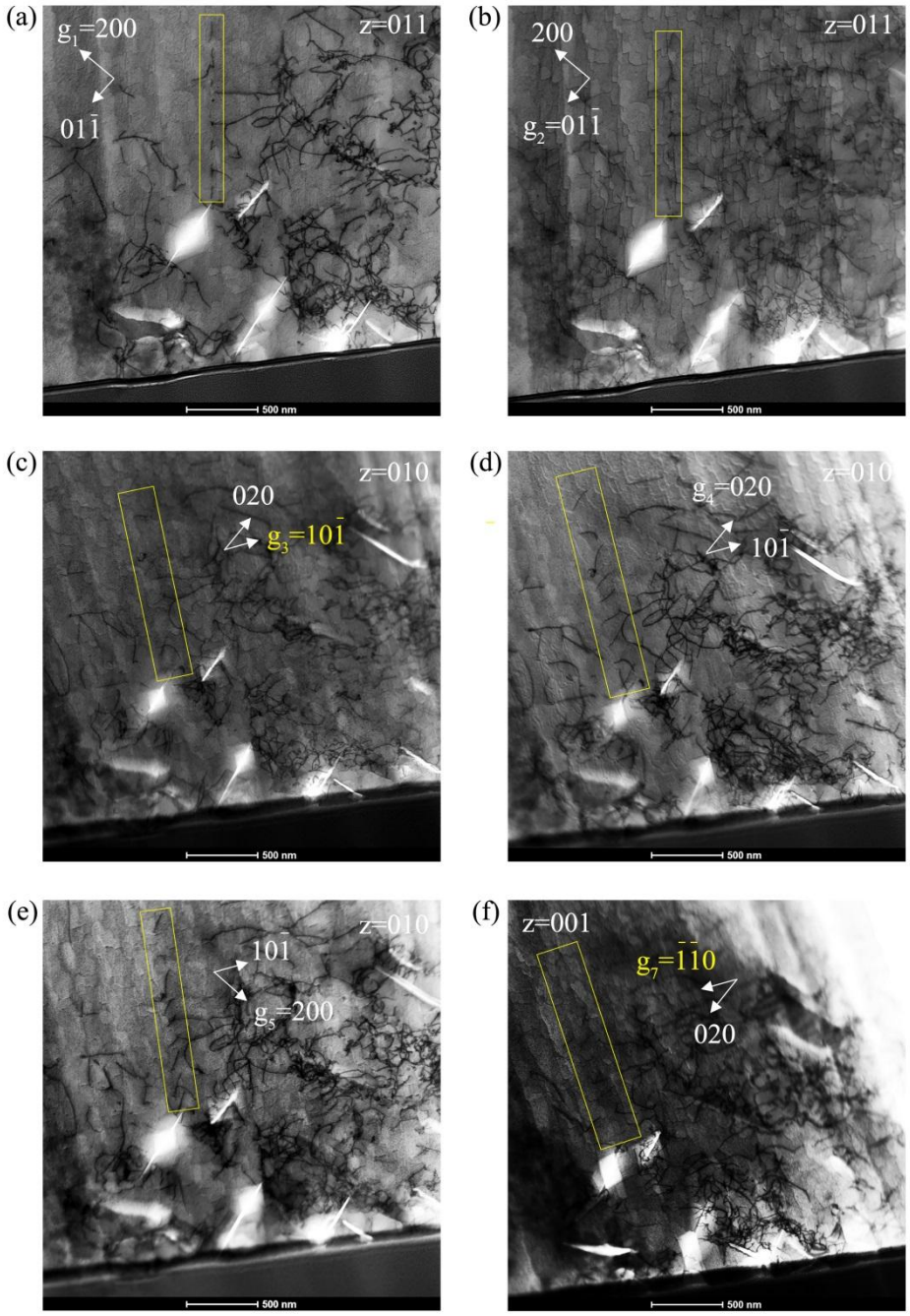

Fig. 5 Morphology of non-edge dislocation loops arrayed at the tip of the cavity along the $[1\bar{1}1]$ direction. The Burgers vector is $\boldsymbol{b_7} = \pm\frac{1}{2}[1\bar{1}1]$ and the slip plane is $(21\bar{1})$. The length of these cavities is about 200-500 nm, which is apparently smaller than the cavities observed in Fig.2-4.

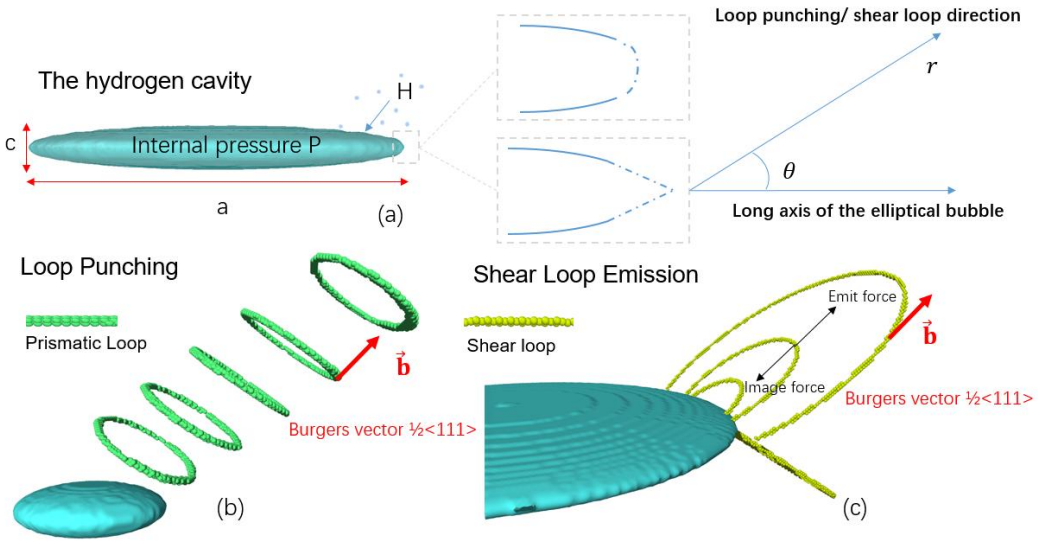

Fig. 6 Schematics for the growth mechanism of H cavities. (a) Structure of the H cavity model and (b) the loop punching mechanism. Driven by the internal gas pressure, prismatic loops are punched out as a chain. The Burgers vector of the punched-out chain of loops is $\pm$1/2<111>, and the sizes of individual loops are similar to that of the cavity. (c) The shear loop emission mechanism. When the cavity is crack-shaped, the dislocations are emitted from the crack tip as gradually expanding shear loops.

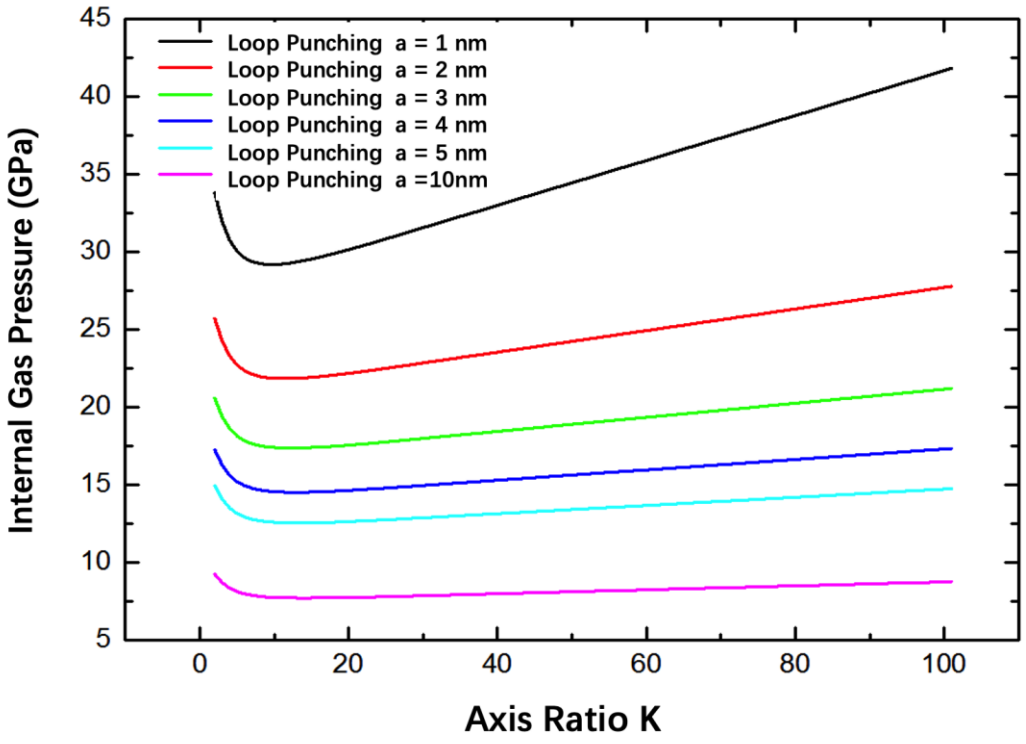

Fig. 7 Internal hydrogen gas pressure required for loop punching from an elliptical cavity with different sizes (a) and axis ratios ($k = a/c$).

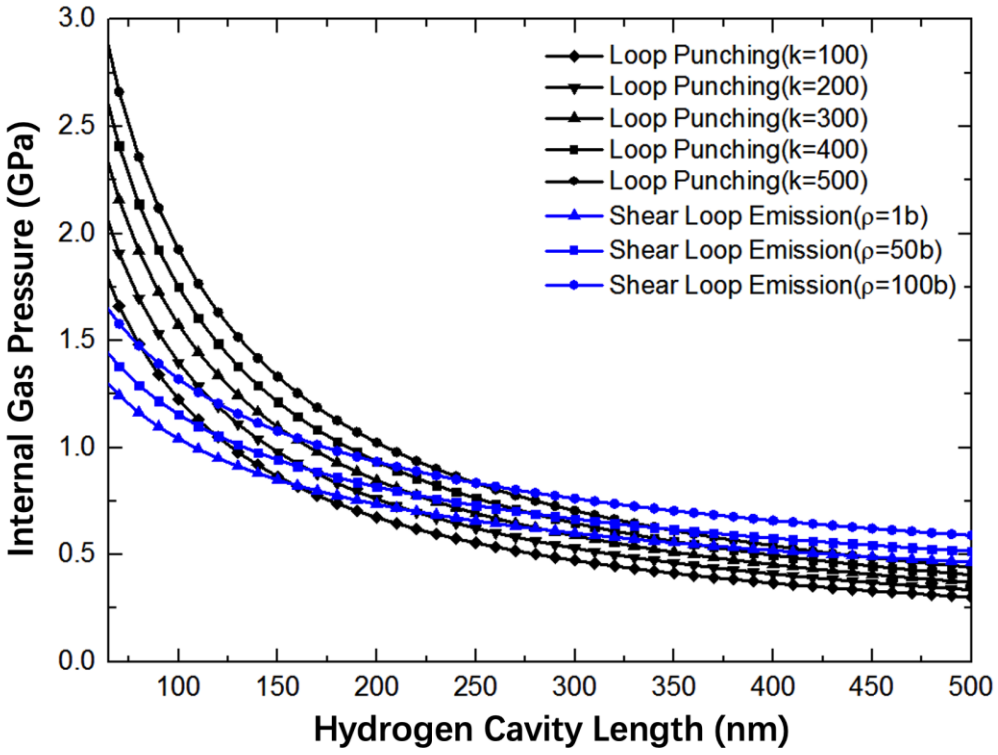

Fig. 8 (Color online) Comparison between the threshold pressure for shear loop emission (blue) and loop punching mechanism (black) at the cavity length of hundreds of nanometers. The mechanism that requires less pressure will be activated first. At this stage, large cavities grow by the loop punching mechanism, while the small cavities grow by the emission of shear loops.

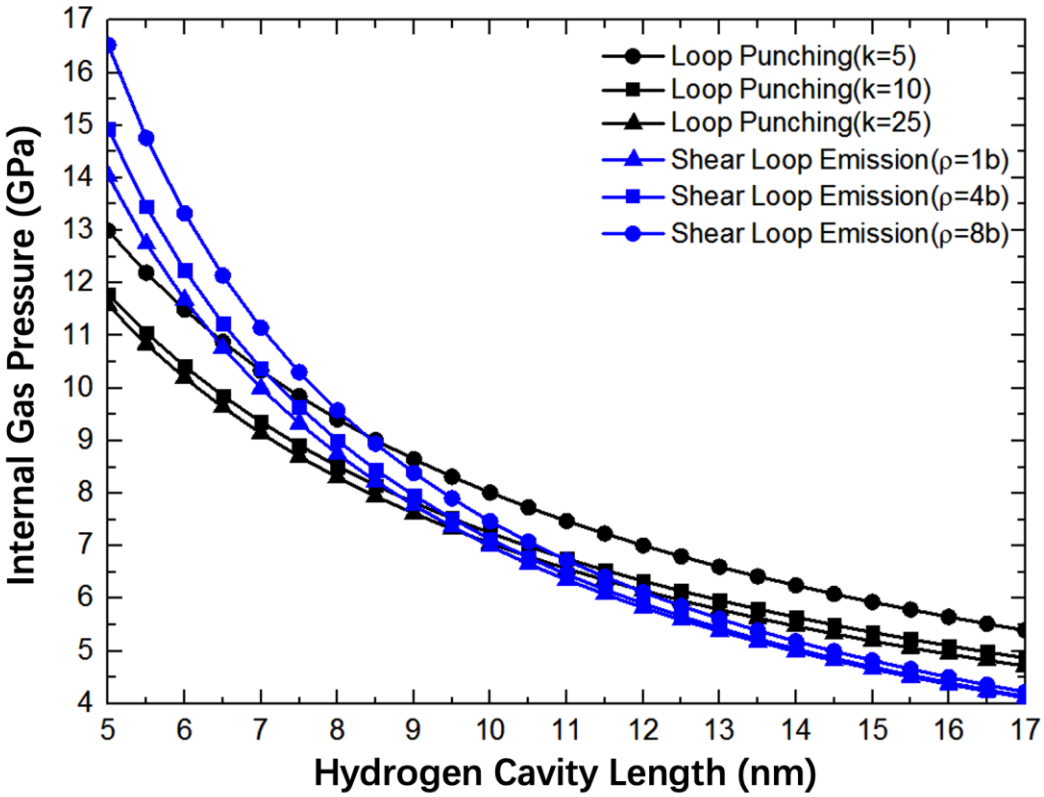

Fig. 9 (Color online) Comparison between the threshold pressure for shear loop emission (blue) and loop punching mechanism (black) with cavities smaller than 20 nm. The mechanism that requires less pressure will be activated first. At this stage, small H cavities grow by punching out nanometer-scale 'coffee-bean' loops, while larger cavities grow by the emission of shear loops.

*Graphical Abstract

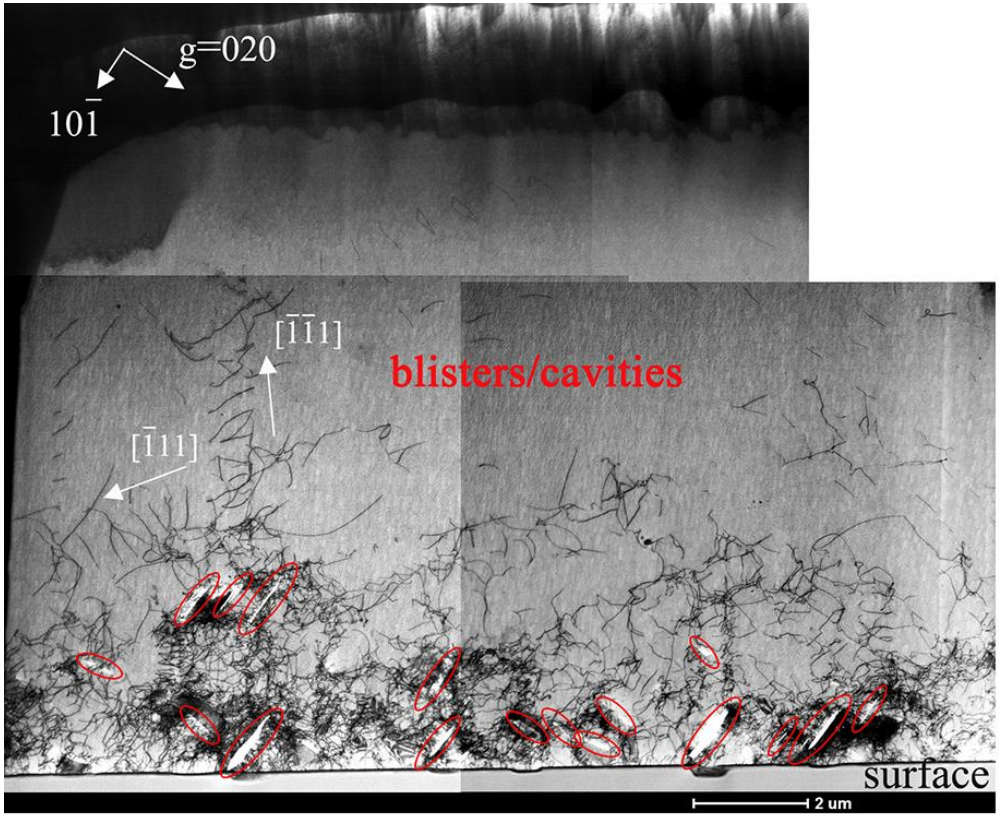

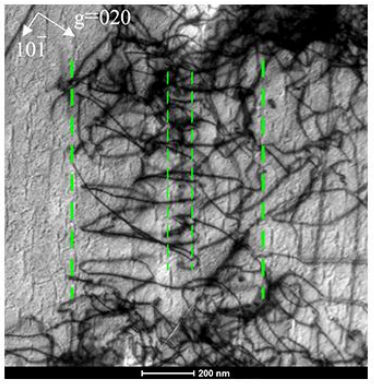

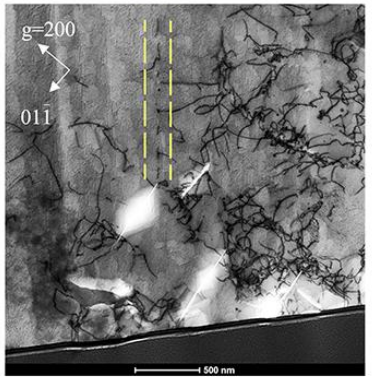

Cross-sectional overview of hydrogen cavities in tungsten

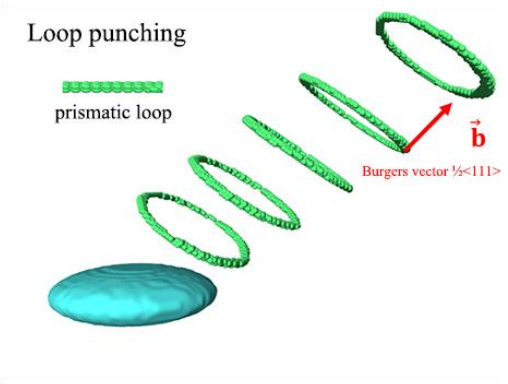

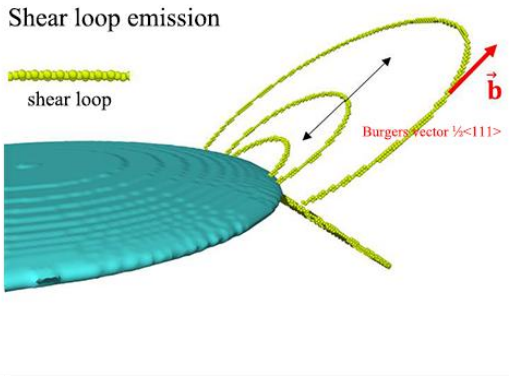

Growth mechanism